
Article:
Huang, L., Feng, J., Guo, S. et al. (2 more authors) (2019) Analysis of power factor in variable flux reluctance machines with MMF-permeance model. IET Electric Power Applications, 13 (5). pp. 614-624. ISSN 1751-8660

https://doi.org/10.1049/iet-epa.2018.5301

Analysis of Power Factor in Variable Flux Reluctance Machines with MMF-Permeance Model

L.R. Huang [1], J.H. Feng [2], S.Y. Guo [2], J.X. Shi [2], Z.Q. Zhu [1*]

[1] Electrical Machines and Drives Group, University of Sheffield, Sheffield S1 3JD, U.K.
[2] CRRC Zhuzhou Institute Co. Ltd, Shidai Road, Shifeng District, Zhuzhou, Hunan, China
[*] z.q.zhu@sheffield.ac.uk

Abstract: This paper investigates the underlying mechanism of low power factor issue of variable flux reluctance machines (VFRMs) from the perspective of MMF-permeance model. Based on a simplified analytical model, the relationship between the design parameters and the power factor is identified and systematically summarized into three predictable ratios: the rotor permeance ratio, stator/rotor pole ratio and DC/AC winding ampere turns ratio. Specifically, the smaller the rotor pole arc, the airgap length, the rotor pole number and the AC/DC winding ampere turns ratio are, the higher the power factor will be. In addition, the weak coupling between the field and armature windings caused by the modulation effect of salient rotor is responsible for the low power factor issue of VFRMs, regardless of the control scheme, winding configuration or saturation effect. A 6-stator-pole/4-rotor-pole VFRM is prototyped and tested for verification.

Nomenclature

A_n	Magnitude of the n-th component of armature modulated MMF.
B_{ga}	Radial airgap flux density due to armature current.
F_a	MMF of armature current.
F_m	Magnitude of the m-th component of field modulated MMF.
F_{sa}	Modulated MMF due to armature current.
F_{sf}	Modulated MMF due to field current.
g_0	Airgap length.
I_a, I_f	The rms values of AC and DC currents.
I_d, I_q	d- and q-axis armature currents.
k_ω	Winding factor.
L_{stk}	Machine stack length.
N_a, N_f	Total turns in series of armature and field windings.
NI_{ratio}	DC/AC winding ampere turns ratio
N_s, N_r	Stator and rotor tooth numbers.
P_a, P_f	Numbers of pole pairs of armature and field windings.
P_{cua}, P_{cuf}	Copper losses of armature and field windings.
pf	Power factor.
P_{ratio}	Stator/rotor pole ratio.
R	Phase resistance.
R_{si}	Radius of stator inner surface.
U	Phase terminal voltage.
W_A	Winding function of phase A.
β_r	Rotor pole arc ratio.
γ_0	Initial rotor position.
θ	Current advance angle.
Λ	Radial airgap permeance.
Λ_r	Radial airgap permeance of rotor-slotted and smooth stator model.
Λ_{r0}	DC component of rotor permeance.
Λ_{ratio}	Rotor permeance ratio.
Λ_{rk}	The k-th component of rotor permeance.
Λ_s	Radial airgap permeance of stator-slotted and smooth rotor model.
μ_0	Vacuum permeability.
φ	Angle between voltage and current vectors.
Φ_{Aa}, Φ_{Af}	Phase A flux linkages when AC or DC current is solely excited.
$\Phi_{Aa\text{-}1}$, $\Phi_{Af\text{-}1}$	Fundamental components of phase A flux linkage when AC or DC is solely excited.
Φ_d, Φ_q	d- and q-axis flux linkages due to armature current.
Φ_f	d-axis flux linkage due to field current.
ω	Electrical rotating speed.
ω_h	The h-th component of winding function of phase A.
Ω_n	Rotating speed of the n-th component of armature modulated MMF.
Ω_r	Mechanical rotating speed.

1. Introduction

With the increasing concerns about the environmental issues, electrical vehicles (EVs) prevails in the market [1]-[4]. As the key device of energy conversion, the electrical machines are of significant importance in EVs. Although permanent magnet (PM) machines are of high priority for the propulsion system due to their excellent performance [5]-[6], many magnetless electrical machines are also re-evaluated recently as alternatives to reduce the manufacture cost [7]-[8].

Variable flux reluctance machines (VFRMs) are one recently developed magnetless machines [9]. The structures of two typical VFRMs with 6-stator-slot/4-rotor-pole (6s/4r) and 6s/5r are shown in Fig. 1. They have double-salient structures, which are similar to those of switched reluctance machines (SRMs) [10]. Two sets of windings, i.e., AC-excited armature winding and DC-excited field winding, are both located in stator, which avoids the requirement of slip-ring/brush and makes it possible to use commercial three-phase inverter. In [11]–[13], the electromagnetic performances of VFRMs have been analyzed in terms of torque capability, stator/rotor pole combination, winding configuration and noise and vibration. Compared with SRMs,

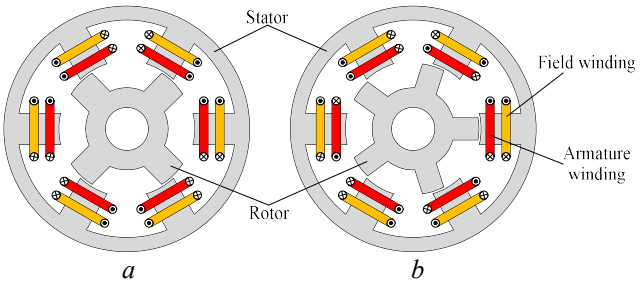

Fig. 1. *Structures of VFRMs.*
(a) 6s/4r VFRM
(b) 6s/5r VFRM

VFRMs have significant advantages on acoustic noise and vibration reduction. In [14], the torque production of VFRMs is explained by flux modulation theory [15]. VFRMs are found to be one stator-wound-field (SWF) synchronous machine. As another important criterion of machine design, the power factor is to be investigated in this paper.

In fact, the power factor is closely related to the inverter capacity requirement of drive system. In [16], the power factors of seven kinds of electric machines are compared for EVs. Synchronous reluctance machines (SynRMs) are found to have relatively lower power factor than many conventional synchronous machines. Then, the analysis of [17] and [18] further states that the vernier reluctance machines (VRMs) have even lower power factor than the SynRMs. In fact, many SWF and stator PM-excited machines, e.g., transverse flux PM machines [19]-[22], flux reversal machines [23], VRMs [24][25], flux-modulated PM machines [26][27], are reported to suffer from low power factor issue at full load condition (<0.55). As another SWF machine, VFRMs may also have the same problem. Hence, it is essential to investigate the power factor in VFRMs.

In existing literature [16]-[27], the power factor analysis is generally based on the inductance calculation. To obtain the inductance, the finite element analysis (FEA) is the most frequently used method. However, since the inductance is actually a synergistic indicator of all the design parameters, the relationship between the design parameters and the power factor cannot be fully explained. For example, in [24], the power factor of DC-excited VRMs is investigated by FEA. The variation trends of power factor with some specific design parameters have been presented based on inductance calculation. Due to the common structure features between DC-excited VRM and VFRM, some conclusions revealed in [24] may also be used in VFRM. However, due to the limit of FEA, the underlying mechanism of the revealed conclusions are still shaded. In [20] and [27], a magnetic equivalent circuit based and a subdomain based analytical methods are proposed for power factor calculation. However, these methods are actually alternative ways of FEA for airgap magnetic field calculation, whereas they fail to explain the relationship between the individual design parameters and the power factor, as well as the nature of low power factor issue.

In this paper, the power factor of VFRMs is analytically analysed based on an MMF-permeance model, which breaks the power factor expression down to the MMF and the airgap permeance. Based on this, the nature of low power factor issue is fully explained by harmonic analysis. Furthermore, with this model, the influence of design parameters on power factor can be separately analysed and is systematically summarized into three predictable ratios, i.e., rotor permeance ratio, stator/rotor pole ratio and DC/AC winding ampere turns ratio, to assist the machine design.

The paper is organized as follows: Firstly, the analytical expressions of the power factor in VFRMs are derived in Section 2. Based on this, the relationship between the design parameters and the power factor is revealed, which is then verified by FEA in Section 3. Then, the nature of the low power factor issue in VFRMs is illustrated in Section 4. In Section 5, a design method considering power factor is introduced for VFRMs. Finally, the experimental results are presented in Section 6.

2. Power Factor of VFRMs

The phasor diagram and general power factor expression of VFRM are identical to those of conventional synchronous machines, as presented in Fig. 2(a).

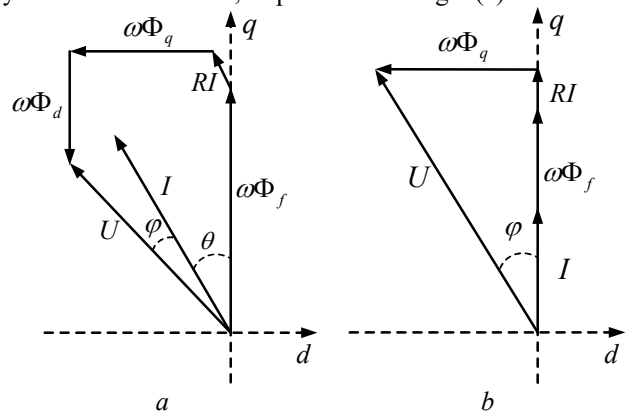

Fig. 2. *Phasor diagrams of VFRMs.*
(a) I_d, $I_q \neq 0$
(b) $I_d = 0$, $I_q \neq 0$

$$pf = \cos\varphi = \cos\left[\arctan\left(\frac{\omega\Phi_q - RI_d}{\omega\left(\Phi_f + \Phi_d\right) + RI_q}\right) - \theta\right] \quad (1)$$

where U is the phase terminal voltage; ω is the electrical rotating speed; (I_d, I_q) are the armature currents of d- and q-axes, respectively; (Φ_d, Φ_q) are the d- and q-axes flux linkages generated by AC current; Φ_f is the d-axis flux linkage generated by DC current; R is the phase resistance; θ is the current advanced angle.

Further, it is confirmed in [11] and [14] that, in a VFRM, the synchronous torque has the dominant contribution in average torque production, whereas the reluctance torque is negligible. For maximal torque operation, the advanced current angle of VFRM is chosen as 0 and I_d=0 scheme is usually applied in the control of VFRM. In this case, the terminal voltage needs to be adjusted to ensure I_d=0 for different load condition. Hence, the power factor will change correspondingly and the phasor diagram is modified to Fig. 2(b). Neglecting the influence of phase resistance for simplicity, the simplified power factor expression is:

$$pf = \frac{1}{\sqrt{1 + \left(\Phi_q / \Phi_f\right)^2}} \quad (2)$$

The power factor of VFRM is found to be closely related to the flux ratio Φ_q/Φ_f. The average value of this ratio over one electrical period can be expressed as

$$\left(\Phi_q/\Phi_f\right)_{avg}=\Phi_{Aa-1}/\Phi_{Af-1} \tag{3}$$

where $\Phi_{Aa\text{-}1}$ and $\Phi_{Af\text{-}1}$ are the fundamental components of phase flux linkages when armature or field winding is solely excited.

It is apparent that smaller $\Phi_{Aa\text{-}1}/\Phi_{Af\text{-}1}$ will lead to larger power factor over one electrical period.

Further, to investigate the relationship between flux ratio $\Phi_{Aa\text{-}1}/\Phi_{Af\text{-}1}$ and design parameters, an analytical model of flux linkage is introduced by using the winding function theory [28], the flux linkage of phase A due to armature current only is:

$$\Phi_{Aa}=R_{si}L_{stk}\int_0^{2\pi}W_A B_{ga}d\theta \tag{4}$$

where R_{si} is the radius of stator inner surface; L_{stk} is the stack length; W_A is the winding function of phase A; B_{ga} is the radial airgap flux density due to armature current and can be calculated by the MMF-permeance model [14][29]:

$$\begin{cases}B_{ga}=F_a\Lambda\\ \Lambda\approx g_0\Lambda_s\Lambda_r/\mu_0\end{cases} \tag{5}$$

where F_a is the MMF of armature current; Λ is the radial airgap permeance; g_0 is the airgap length; μ_0 is the vacuum permeability; Λ_s is the radial airgap permeance of stator-slotted and smooth rotor model; Λ_r is the radial airgap permeance of rotor-slotted and smooth stator model.

By substituting (5) into (4), Φ_{Aa} can be expressed as:

$$\Phi_{Aa}=R_{si}L_{stk}\int_0^{2\pi}W_A\left(F_a g_0\Lambda_s/\mu_0\right)\Lambda_r d\theta=R_{si}L_{stk}\int_0^{2\pi}W_A F_{sa}\Lambda_r d\theta \tag{6}$$

where F_{sa} is defined as the "modulated MMF", which is the equivalent MMF modulated by stator slotting effect. As confirmed in [14], the modulated MMF has identical harmonic content as the original MMF without stator slotting effect, albeit with modified harmonic magnitudes due to the introduction of stator permeance Λ_s. By using (5) and (6), the stator and rotor permeances are separated and the effect of stator permeance is included in the modulated MMF.

Similarly, the flux linkage of phase A due to field current can also be obtained:

$$\Phi_{Af}=R_{si}L_{stk}\int_0^{2\pi}W_A F_{sf}\Lambda_r d\theta \tag{7}$$

where F_{sf} is the modulated MMF of field current.

In (6) and (7), W_A, F_{sa}, F_{sf} and Λ_r are four coefficients to be determined. For VFRMs, their general expressions are:

$$W_A=\sum_{h=1}^{\infty}\omega_h\cos\left(h\theta\right) \tag{8}$$

$$F_{sa}=\sum_{n\neq3,6,9...}^{\infty}A_n\cos\left(n\theta-\Omega_n t\right),\ \Omega_n=\pm N_r\Omega_r \tag{9}$$

$$F_{sf}=\sum_{m=1,3,5...}^{\infty}F_m\cos\left(m\theta\right) \tag{10}$$

$$\Lambda_r=\Lambda_{r0}+\sum_{k=1,2,3...}\Lambda_{rk}\cos\left[kN_r\left(\theta-\Omega_r t+\gamma_0\right)\right] \tag{11}$$

where ω_h is the magnitude of the h-th component of winding function of phase A; A_n and Ω_n are the magnitude and rotating speed of the n-th component of armature modulated MMF, respectively; F_m is the magnitude of the m-th component of field modulated MMF; N_s and N_r are the stator and rotor tooth numbers, respectively; Λ_{r0} and Λ_{rk} are the dc and k-th components of rotor permeance; Ω_r is the mechanical rotating speed of rotor; γ_0 is the initial rotor position.

By substituting (8)-(11) into (6) and (7), the flux linkages of phase A due to field and armature currents can be obtained:

$$\Phi_{Af}=R_{si}L_{stk}\int_0^{2\pi}W_A F_{sf}\Lambda_r d\theta$$
$$=\left\{\begin{array}{l}R_{si}L_{stk}\pi\sum\limits_{h=\frac{mN_s}{2}}^{\infty}\sum\limits_{m=1,3,5...}^{\infty}\omega_h F_m\Lambda_{r0}+\\ \dfrac{R_{si}L_{stk}\pi}{2}\sum\limits_{h=\left|m\pm kN_r\right|}\sum\limits_{m=1,3,5...}^{\infty}\sum\limits_{k=1,2,3...}^{\infty}\omega_h F_m\Lambda_{rk}\cos\left(kN_r\Omega_r t-kN_r\gamma_0\right)\end{array}\right\} \tag{12}$$

$$\Phi_{Aa}=R_{si}L_{stk}\int_0^{2\pi}W_A F_{sa}\Lambda_r d\theta$$
$$=\left\{\begin{array}{l}R_{si}L_{stk}\pi\sum\limits_{h=n}^{\infty}\sum\limits_{n\neq3,6,9...}^{\infty}\omega_h A_n\Lambda_{r0}\cos\left(\Omega_n t\right)+\\ \dfrac{R_{si}L_{stk}\pi}{2}\sum\limits_{h=n+kN_r}\sum\limits_{n\neq3,6,9...}^{\infty}\sum\limits_{k=1,2,3...}^{\infty}\omega_h A_n\Lambda_{rk}\cos\left[\left(\Omega_n+kN_r\Omega_r\right)t-kN_r\gamma_0\right]+\\ \dfrac{R_{si}L_{stk}\pi}{2}\sum\limits_{h=\left|n-kN_r\right|}\sum\limits_{n\neq3,6,9...}^{\infty}\sum\limits_{k=1,2,3...}^{\infty}\omega_h A_n\Lambda_{rk}\cos\left[\left(\Omega_n-kN_r\Omega_r\right)t+kN_r\gamma_0\right]\end{array}\right\} \tag{13}$$

Since the dc and 1st components are the dominant ones for the airgap permeance for a regular rotor [14][26], the components in (12) and (13), which are associated with ≥2nd order rotor permeance harmonics, can be neglected, yielding:

$$\Phi_{Aa-1}=\Lambda_{r0}R_{si}L_{stk}\pi\sum_{h=n}^{\infty}\sum_{n\neq3,6,9...}^{\infty}\omega_h A_n\cos\left(N_r\Omega_r t\right) \tag{14}$$

$$\Phi_{Af-1}=\frac{1}{2}\times\Lambda_{r1}R_{si}L_{stk}\pi\sum_{h=\left|m\pm N_r\right|}\sum_{m=1,3,5...}^{\infty}\omega_h F_m\cos\left(N_r\Omega_r t-N_r\gamma_0\right) \tag{15}$$

It can be seen that $\Phi_{Aa\text{-}1}$ and $\Phi_{Af\text{-}1}$ are proportional to the dc and fundamental rotor permeance components, respectively. Consequently, the flux ratio of VFRMs is:

$$\frac{\Phi_{Aa-1}}{\Phi_{Af-1}}=\frac{2\Lambda_{r0}}{\Lambda_{r1}}\times\frac{\sum\limits_{h=n}^{\infty}\sum\limits_{n\neq3,6,9...}^{\infty}\omega_h A_n}{\sum\limits_{h=\left|m\pm N_r\right|}\sum\limits_{m=1,3,5...}^{\infty}\omega_h F_m} \tag{16}$$

The power factor can be evaluated by:

$$pf=\frac{1}{\sqrt{1+\left(\dfrac{\Phi_{Aa-1}}{\Phi_{Af-1}}\right)^2}}=\frac{1}{\sqrt{1+\left(\dfrac{2\Lambda_{r0}}{\Lambda_{r1}}\times\dfrac{\sum\limits_{h=n}^{\infty}\sum\limits_{n\neq3,6,9...}^{\infty}\omega_h A_n}{\sum\limits_{h=\left|m\pm N_r\right|}\sum\limits_{m=1,3,5...}^{\infty}\omega_h F_m}\right)^2}} \tag{17}$$

It is known that the magnitudes of the harmonics of both modulated MMFs and winding functions are decreasing with their order number [28]. By only considering the dominant components of modulated MMFs and winding functions, (16) can be further simplified into

$$\frac{\Phi_{Aa-1}}{\Phi_{Af-1}}\approx\frac{2\Lambda_{r0}}{\Lambda_{r1}}\times\frac{\omega_{P_a}A_{P_a}+\omega_{\left|N_s-P_a\right|}A_{\left|N_s-P_a\right|}}{\omega_{\left|P_f-N_r\right|}F_{P_f}} \tag{18}$$

where P_a and P_f are the pole pairs of armature and field windings, respectively.

From the winding theory, the magnitudes of the harmonics of modulated MMF and winding functions are governed by:

$$\begin{cases}\omega_h\propto k_\omega/h\\ A_n\propto k_\omega N_a I_a/n\\ F_m\propto N_f I_f/m\end{cases} \tag{19}$$

where N_a and N_f are the total turns in series of armature and field windings; I_a and I_f are the rms values of AC and DC currents; k_ω is the winding factor.

By using (19), expression (18) can be rewritten into

$$\frac{\Phi_{Aa-1}}{\Phi_{Af-1}}\propto\frac{\Lambda_{r0}}{\Lambda_{r1}}\times k_\omega\left(\frac{\dfrac{1}{P_a^2}+\dfrac{1}{\left|N_s-P_a\right|^2}}{\dfrac{1}{\left|P_f-N_r\right|P_f}}\right)\times\frac{N_a I_a}{N_f I_f} \tag{20}$$

Consequently, since the power factor is inversely correlated to the flux ratio, the relationship between power factor and design parameters can be expressed as:

$$pf \propto \frac{\Lambda_{r1}}{\Lambda_{r0}} \times \frac{\frac{1}{\left|P_f - N_r\right|P_f}}{k_\omega \left(\frac{1}{P_a^2} + \frac{1}{\left|N_s - P_a\right|^2} \right)} \times \frac{N_f I_f}{N_a I_a} \tag{21}$$
$$= \Lambda_{ratio} \times P_{ratio} \times NI_{ratio}$$

From (21), it can be seen that the power factor of VFRMs are influenced by three independent factors, i.e., rotor permeance ratio Λ_{ratio}, stator/rotor pole ratio P_{ratio} and DC/AC winding ampere turns ratio NI_{ratio}. This conclusion will be verified by FEA results afterwards in Section III.

3. FEA Verification

In this section, the revealed features of power factor in Section II will be verified by the FEA results of a 6s/4r VFRM and a 6s/5r VFRM. Their configurations and main specifications are shown in Fig. 1 and Table 1, respectively. The FEA results presented in this paper are obtained with the ANSYS Maxwell 18.2 software and 2D analysis.

Table 1 Main specifications of 6s/4r and 6s/5r VFRMs

Parameters	Unit	VFRM	
		6s/4r	6s/5r
Stator outer diameter	mm	90	
Total copper loss	W	30	
Turns per slot (AC/DC)	-	183/183	
Split ratio	-	0.5	
Rotor outer diameter	mm	45	
Stator pole arc	deg.	30	

3.1. Rotor Permeance Ratio

The rotor permeance ratio Λ_{ratio} is defined as:

$$\Lambda_{ratio} = \frac{\Lambda_{r1}}{\Lambda_{r0}} \tag{22}$$

According to (21), the larger the Λ_{ratio} is, the higher the power factor will be. The magnitudes of the dc and 1st rotor permeance components are mainly determined by two design parameters, i.e., the rotor pole arc ratio β_r (rotor pole arc divided by rotor tooth pitch) and airgap length g_0 [29].

Firstly, the airgap length is fixed to 0.5mm. The variations of rotor permeance with rotor pole arc are obtained by the method proposed in [14], as shown in Fig. 3. It can be found that $\Lambda_{r1}/\Lambda_{r0}$ is continuously decreasing with the rotor pole arc ratio, which means the power factor of VFRMs will also decrease with the rotor pole arc. To verify this, the variations of the flux linkages and power factor with rotor pole arc ratio are presented in Figs. 3(b) and (c). To clearly compare the variation trends, the per-unit values of flux linkage and rotor permeance are presented in Fig. 3(b) with their values when rotor pole arc ratio is 0.56 are chosen as the baselines. As expected, the phase flux linkages due to armature and field currents alone are proportional to the dc and 1st rotor permeance components, respectively. Moreover, the larger the rotor pole arc ratio is, the lower the power factor of VFRMs will be.

Further, the influence of airgap length is accounted for. The rotor pole arc ratio is fixed to 0.44. Fig. 4(a) shows the variations of rotor permeance with airgap length. Fig. 4(b) shows the variations of per-unit values of Λ_{r0} and Λ_{r1}, flux linkage with their values when airgap length is 0.25mm are

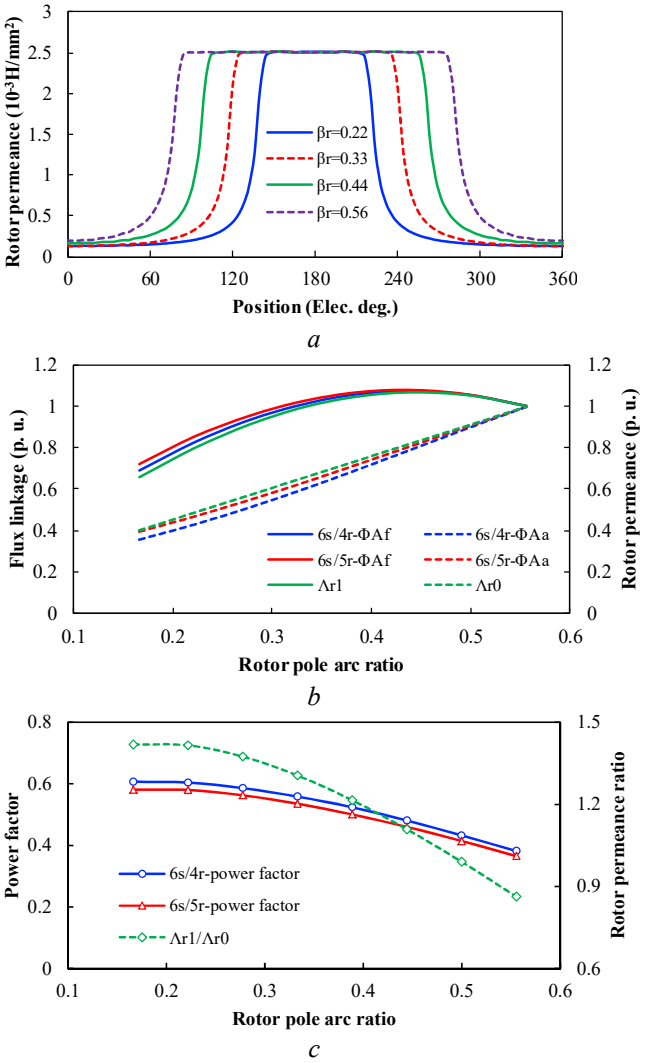

Fig. 3. *Distributions of rotor permeance over one rotor pole and variations of Λ_{r0}, Λ_{r1}, flux linkage and power factor under different rotor pole arc ratio (g_0=0.5mm).*
(a) *Rotor permeance distributions*
(b) *Variations of Λ_{r0}, Λ_{r1} and flux linkage*
(c) *Power factor and rotor permeance ratio $\Lambda_{r1}/\Lambda_{r0}$*

chosen as the baseline. The Λ_{r0}, Λ_{r1} and $\Lambda_{r1}/\Lambda_{r0}$ are decreasing with the expansion of airgap, so is the power factor, as confirmed in Fig. 4(c).

Overall, the smaller the rotor pole arc ratio and airgap length are, the higher the power factor of VFRMs will be.

3.2. Stator/Rotor Pole Ratio

The stator/rotor pole ratio is defined as:

$$P_{ratio} = \frac{\frac{1}{\left|P_f - N_r\right|P_f}}{k_\omega \left(\frac{1}{P_a^2} + \frac{1}{\left|N_s - P_a\right|^2} \right)} \tag{23}$$

Table 2 shows the feasible stator/rotor pole combinations of 6-and 12-stator slots VFRMs and their corresponding pole ratios. As can be seen, the stator/rotor pole ratio shows a decreasing trend with the rotor pole number. Hence, the power factor is also expected to decrease with the rotor pole number. To verify this, the 6s- and 12s-VFRMs having (2, 4, 5…20) rotor pole numbers are designed with the constraints listed in Table 1 to achieve peak average

torque. Meanwhile, the rotor pole ratio, airgap length and DC/AC ampere turns ratio are fixed to 0.38, 0.5mm and 1, respectively, to avoid mutual influence from rotor permeance and DC/AC ampere turns ratios. The variations of power factor and stator/rotor pole ratio with rotor pole number match the expectations, as shown in Fig. 5.

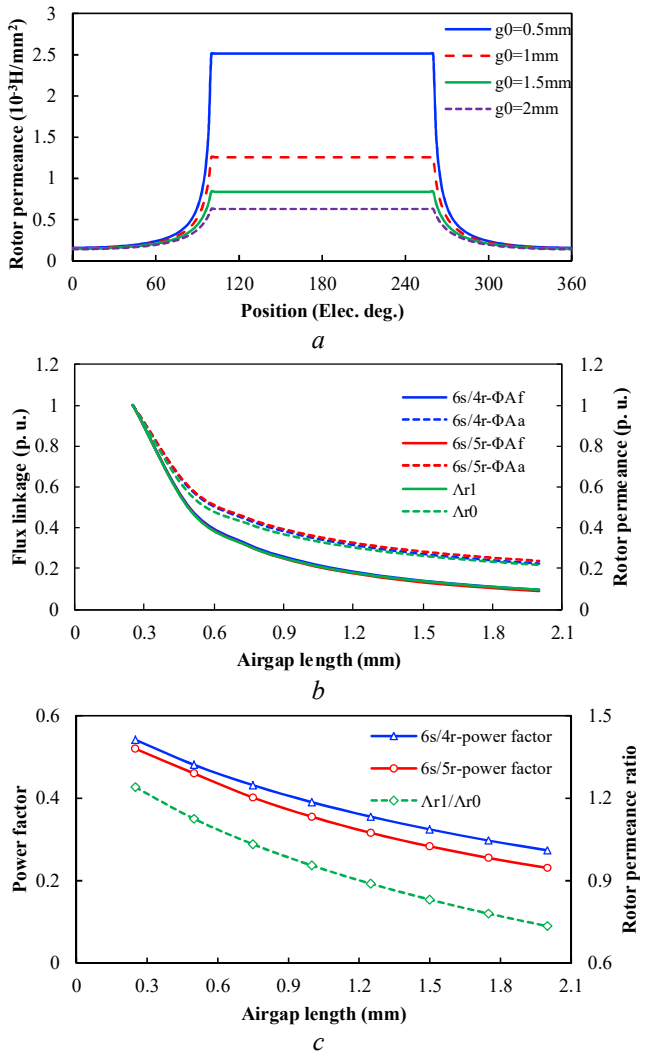

Fig. 4. *Distributions of rotor permeance over one rotor pole and variations of Λ_{r0} and Λ_{r1}, flux linkage and power factor under different airgap length (β_r=0.44, P_{cua}=P_{cuf}=15W).*
(a) *Rotor permeance distributions*
(b) *Variations of Λ_{r0}, Λ_{r1} and flux linkage*
(c) *Power factor and rotor permeance ratio $\Lambda_{r1}/\Lambda_{r0}$*

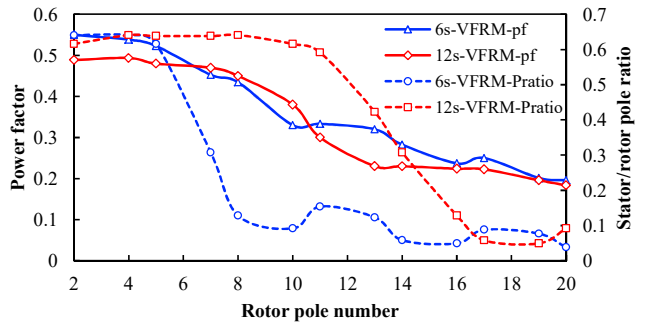

Fig. 5. *Variations of power factor and stator/rotor pole ratio with rotor pole number for 6s- and 12s-VFRMs (P_{cua}=P_{cuf}=15W).*

Table 2 Feasible stator/rotor pole combinations and their corresponding pole ratios for 6s- and 12s- VFRMs

VFRMs	N_s	N_r	P_a	P_f	k_ω	P_{ratio}
6s/2r	6	2	1	3	0.5	0.641
6s/4r		4	1		0.5	0.641
6s/5r		5	2		0.866	0.616
6s/7r		7	2		0.866	0.308
6s/8r		8	1		0.5	0.128
6s/10r		10	1		0.5	0.092
6s/11r		11	2		0.866	0.154
6s/13r		13	2		0.866	0.123
6s/14r		14	1		0.5	0.058
6s/16r		16	1		0.5	0.049
6s/17r		17	2		0.866	0.088
6s/19r		19	2		0.866	0.077
6s/20r		20	1		0.5	0.038
12s/2r	12	2	4	6	0.866	0.616
12s/4r		4	2		0.5	0.641
12s/5r		5	1		0.259	0.638
12s/7r		7	1		0.259	0.638
12s/8r		8	2		0.5	0.641
12s/10r		10	4		0.866	0.616
12s/11r		11	5		0.933	0.591
12s/13r		13	5		0.933	0.422
12s/14r		14	4		0.866	0.308
12s/16r		16	2		0.5	0.128
12s/17r		17	1		0.259	0.058
12s/19r		19	1		0.259	0.049
12s/20r		20	2		0.5	0.092

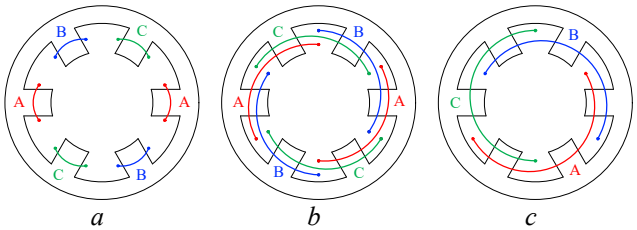

Fig. 6. *Armature winding with concentrated and distributed configurations.*
(a) *Concentrated winding*
(b) *Distributed winding I (coil pitch=2)*
(c) *Distributed winding II (coil pitch=3).*

Table 3 Winding factor of 6s/4r VFRM with armature winding having different coil pitch

Winding type	Coil pitch	Pitch factor	Distributed factor	Winding factor
		k_p	k_d	k_ω
Concentrated winding	1	0.5	1	0.5
Distributed winding	2	0.866	1	0.866
	3	1	1	1

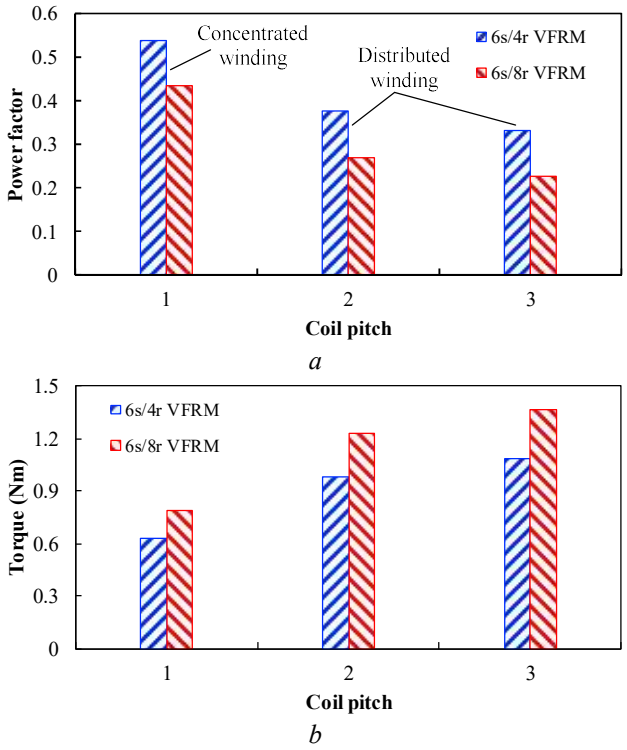

Fig. 7. *Comparison of power factors and output torque of 6s/4r and 6s/8r VFRMs with concentrated and distributed windings (P_{cua}=P_{cuf}=15W).*
(a) *Power factor*
(b) *Output torque*

It is worth noticing that the conclusion mentioned above applies to all the VFRMs with concentrated armature winding. In fact, the distributed winding is also applicable to some specific VFRMs, e.g., 6s/4r and 6s/8r VFRMs. The configurations of concentrated and distributed windings are shown in Fig. 6. These two winding types have identical harmonic content, albeit with different winding factors, as shown in Table 3. The pitch factor of concentrated winding is smaller than that of distributed winding. According to (23), the stator/rotor pole ratios of VFRMs with concentrated winding are therefore larger than those with distributed winding, so is the power factor, as confirmed in Fig. 7(a). However, the higher power factor of concentrated winding does not necessarily lead to a higher output power. Due to the higher winding factor, the machines with distributed winding has significantly larger torque/copper loss ratio than those with concentrated winding, as confirmed by the FEA results in Fig. 7(b). Overall, the concentrated winding is able to improve the power factor and the usage of inverter capacity, whereas the distributed windings are much better in terms of torque/copper loss ratio.

3.3. DC/AC Winding Ampere Turns Ratio

The DC/AC winding ampere turns ratio is defined by

$$NI_{ratio} = \frac{N_f I_f}{N_a I_a} \tag{24}$$

Assuming the slot areas occupied by field and armature winding are equal, the DC/AC ampere turns ratio can also be expressed by a ratio of copper loss, i.e.

$$NI_{ratio} = \sqrt{\frac{P_{cuf}}{P_{cua}}} \tag{25}$$

where P_{cuf} and P_{cua} are the copper losses of field and armature windings, respectively.

A higher DC/AC winding ampere turns ratio will lead to a smaller flux ratio and higher power factor. However, it is also proved in [11] that the highest torque/copper loss ratio of VFRM is obtained only when P_{cuf} / P_{cua}=1. Hence, although the power factor can be enhanced by increasing the DC/AC ampere turns ratio, a sacrifice in torque/copper loss ratio is inevitable, as confirmed by the FEA results in Fig. 8.

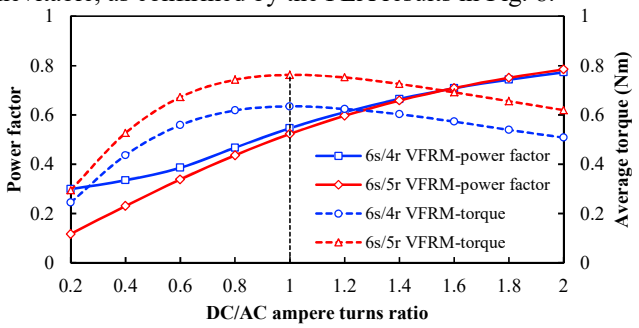

Fig. 8. *Variations of power factor and average torque against DC/AC winding ampere turns ratio for 6s/4r and 6s/5r VFRMs (P_{cu}=30W).*

4. Nature of Low Power Factor Issue In VFRMs

In foregoing investigation, it is proved that the power factor of VFRMs can be enhanced by using smaller rotor pole arc ratio, airgap length and rotor pole number during design. However, the power factor is still lower than 0.6 by adjusting these three parameters, as can be seen from Figs. 3, 4, and 5. This is mainly due to the fact that the ranges of the rotor permeance ratio and stator/rotor pole ratio are quite limited, usually within (0.8~1.4) and (0~0.7), respectively, as confirmed in Figs. 3(c), 4(c) and 5. In contrast, the DC/AC ampere turns ratio is adjustable from 0 to +∞. Therefore, the most effective way for power factor regulation is adjusting the DC/AC ampere turns ratio, albeit with degraded torque/copper loss ratio when NI_{ratio} is not 1. Overall, the power factor of VFRMs is relatively low.

The nature of the low power factor issue lies in the weak coupling between field and armature windings for VFRMs. As can be seen in (15), $\Phi_{Af\text{-}1}$ is generated by the modulation effect of the 1st rotor permeance component. As a result, there is an additional constant coefficient 1/2 in the expression (15), which does not exist in the expression of $\Phi_{Aa\text{-}1}$ (14). From Figs. 3 and 4, it can be seen that the Λ_{ratio} is smaller than 2 (usually within 0.8~1.4). Consequently, as can seen from (16), $\Phi_{Af\text{-}1}$ is usually smaller than $\Phi_{Aa\text{-}1}$ for VFRMs unless the electrical load of field winding is much larger than that of armature winding. In contrast, in a regular rotor-wound-field synchronous machine (RWFSM), $\Phi_{Af\text{-}1}$ is normally larger than $\Phi_{Aa\text{-}1}$ [24]. Hence, the flux ratio of VFRMs is larger than that of RWFSMs, which eventually results in the low power factor issue of VFRMs. Moreover, this conclusion is always valid regardless of control scheme (open-winding control scheme [30] for example), winding configuration (concentrated and distributed windings) and saturation effect since the rotor modulation effect is the basic operation principle of VFRMs [14].

5. Design of VFRM considering power factor

In the foregoing investigation, the influence of three independent factors on power factor is investigated without setting any restrictions on the variation ranges of design parameters. The purpose is to reveal the general relationship between the power factor and the design parameters. However, for a practical machine design, not only power factor, but also output torque, efficiency, electric load, current density and inverter voltage/current /frequency limit need to be taken into account. Hence, the variation ranges of the design parameters will be constrained. For example, the rotor pole arc ratio should vary within (0.33~0.44) to ensure a high torque density [31]. The airgap length is determined by the mechanical constraint. The rotor pole number is constrained by the allowed inverter frequency and peak operation speed. The AC and DC currents are constrained by the allowance of electric load. In addition, the maximal torque/copper loss ratio is achieved when NI_{ratio}=1 [11].

Considering all these constraints, the most frequently used design strategy of VFRMs is based on the global optimization method of structure parameters with NI_{ratio}=1. Maximizing output torque and efficiency are usually chosen as the objectives of the design [9][11][31]. However, for a design with a given inverter capacity and thermal constraint, a fixed NI_{ratio} may lead to a low power factor and low usage of inverter capacity. To further take the power factor into account during design, an adjustable NI_{ratio} can be applied during design, as will be presented in this section.

The design constraints and variables are shown in Table 4. It should be noted that the introduced method is applicable to VFRM designs under different power scale due to the common features in power factor. In this paper, a 90kW machine is selected as an example. According to the inverter frequency allowance and peak speed, the rotor pole number can be chosen up to 5. Since the 6s/5r VFRM has unbalance magnetic force [11], 6s/4r is chosen as the stator/rotor pole combination for this design. By using global optimization method and genetic algorithm in ANSYS Maxwell, two 6s/4r VFRMs are designed to achieve the maximal output power, efficiency and power factor with and without NI_{ratio} fixed to 1. To reduce the copper loss and boost the operation speed range, the open-winding control scheme is applied [30]. Since the operation temperature is hard to obtain, the peak current density and electric load constraints are applied instead. Fig. 9 shows the cross-sections of the globally optimized machines, with their specifications compared in Table 5. The machine with $NI_{ratio}\neq1$ (VFRM II) has smaller split ratio and larger electric load than that with NI_{ratio}=1 (VFRM I).

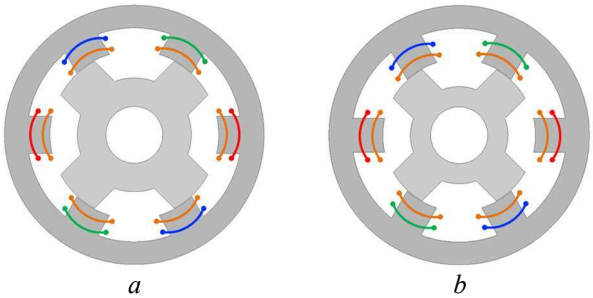

a *b*

Fig. 9. *Cross sections of optimized 6s/4r VFRMs with and without NIratio fixed to 1.*
(a) *NI_{ratio} =1 (VFRM I).*
(b) *NI_{ratio} =1.47 (VFRM II).*

Table 4 Design constraints and variables of 6s/4r VFRMs

Constraints	Unit	Value
Inverter output voltage limitation	V	380
Inverter output current limitation	A	200
Inverter output frequency limitation	Hz	500
Stator outer diameter	mm	365
Stack length	mm	50.8
Airgap length	mm	1
Highest speed of constant torque operation	rpm	2165
Highest speed	rpm	6000
Peak slot current density limitation	A/mm^2	10
Peak electric load limitation	kA/m	100
Optimization variables	**Unit**	**Range**
Split ratio	-	0.5~0.7
Stator pole arc ratio	-	0.33~0.5
Rotor pole arc ratio	-	0.33~0.44
Rotor outer diameter	-	182.5~255.5
Coil turns number	-	30~60
DC/AC ampere turns ratio	-	1~2
Stator yoke thickness	mm	20~40
Rotor yoke thickness	mm	20~40

Table 5 Design parameters of 6s/4r VFRMs

Variables	Unit	6s/4r VFRMs	
		NI_{ratio} =1	$NI_{ratio}\neq1$
Split ratio	-	0.65	0.59
Stator pole arc ratio	-	0.45	0.43
Rotor pole arc ratio	-	0.36	0.35
Coil turns number	-	35	52
NI_{ratio}	-	1	1.47
Stator yoke thickness	mm	29	31
Rotor yoke thickness	mm	40	30
Current density	A/mm^2	9.8	10
Electric load	kA/m	56.5	92.8

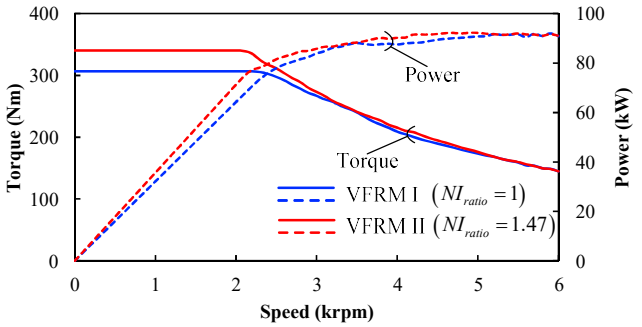

Fig. 10. *Torque/power-speed curves of 6s/4r VFRM with and without NI_{ratio} fixed to 1.*

A comparison of the torque/power-speed curves of these two machines are also calculated, as shown in Fig. 10. The peak output torque of VFRM II (340Nm) is significantly larger than that of VFRM I (306Nm), an 11% increase. This is mainly owing to the improvement of the power factor of the peak torque operation region when NI_{ratio} >1, as can be seen from Fig. 11. Fig. 12 further presents the efficiency maps of designed VFRMs. Although VFRM II has larger copper loss than VFRM I, the higher output power of VFRM II assigns it with equivalent efficiency as VFRM I. Also, this reveals the fact that the power factor is closely related to the output power, whereas the efficiency is also relevant to the loss level. A high power factor is not necessarily lead to a high efficiency in VFRMs.

Overall, by using NI_{ratio}>1 strategy during design, the power factor and peak torque of VFRMs can be effectively boosted under a given inverter capacity.

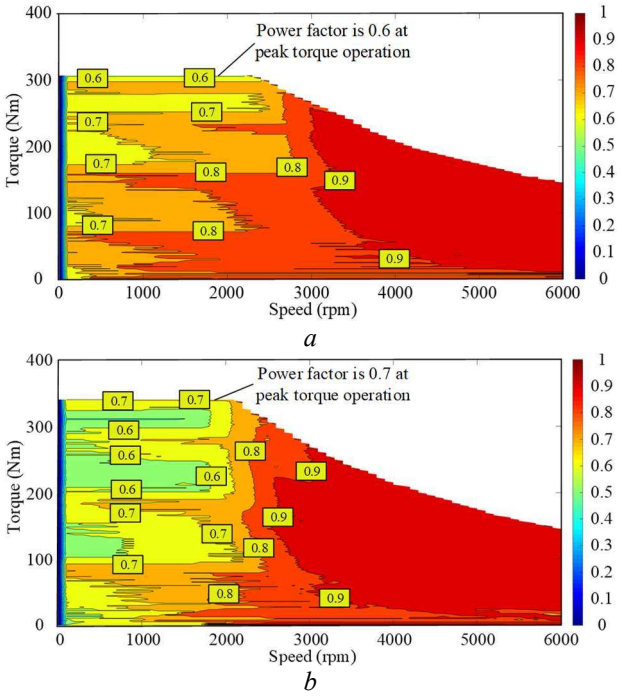

Fig. 11. *Distributions of power factor of all the operation points on efficiency maps of 6s/4r VFRMs with and without NI_{ratio} fixed to 1.*
(a) *VFRM I.*
(b) *VFRM II.*

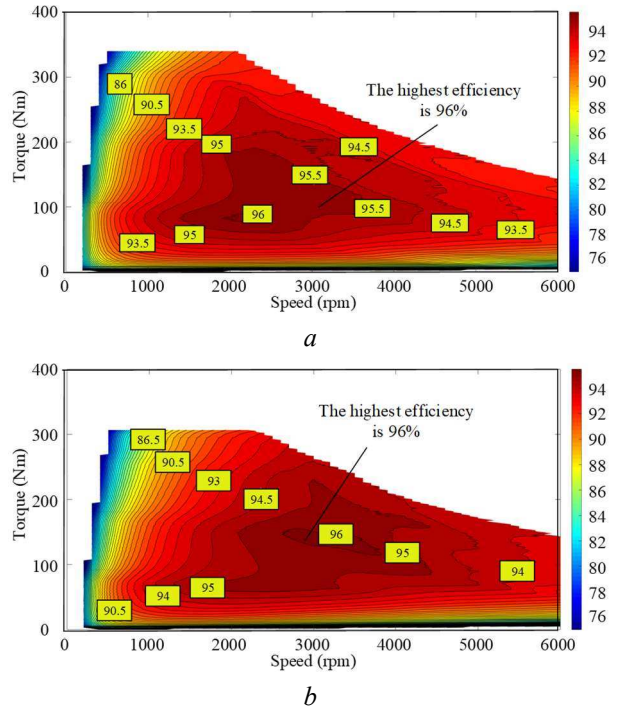

Fig. 12. *Efficiency maps of 6s/4r VFRMs with and without NIratio fixed to 1.*
(a) *VFRM I.*
(b) *VFRM II.*

6. Experimental Verification

For verification, a 6s/4r VFRM is prototyped, as shown in Fig. 13. The main specifications are listed in Table 6. The AC current is excited by a commercial inverter and the DC current is supplied by a DC power supply. The test rig is shown in Fig. 14.

Firstly, by using the LCR meter, the inductance of the prototype can be measured. The FEA calculated and measured peak values of the armature self-inductance and mutual inductance between armature and field windings are compared in Table 7. The measured data is slightly smaller than the prediction, which is mainly due to the measurement error. It shows that due to the aforementioned modulation effect of rotor, the mutual inductance is equivalent to the self-inductance, which will lead to a low factor in the prototype.

Fig. 15 then shows the measured back-EMFs at 1A and 2A DC currents. The measurements match the FEA results well. Fig. 16 further shows the variation of average torque with total RMS current. To maintain the maximal torque/copper loss ratio, the DC/AC ampere turns ratio is kept as 1. The measurement is slightly smaller than FEA prediction due to the evitable measurement error and end effect of windings.

Table 6 Main specifications of prototype 6s/4r VFRM

Parameter	Value	Parameter	Value
Number of phases	3	Stator outer diameter	90mm
DC-bus voltage	48V	Rotor outer diameter	46.4 mm
Split ratio	0.52	Airgap length	0.5mm
Stator pole arc	30 deg.	Rotor pole arc	41 deg.
Rated speed	400rpm	Turns per coil (AC/DC)	183/183
Stack length	25mm	Phase resistance	6.2 Ohm

Fig. 13. *Photos of 6s/4r VFRM prototype.*
(a) *Stator*
(b) *Rotor*

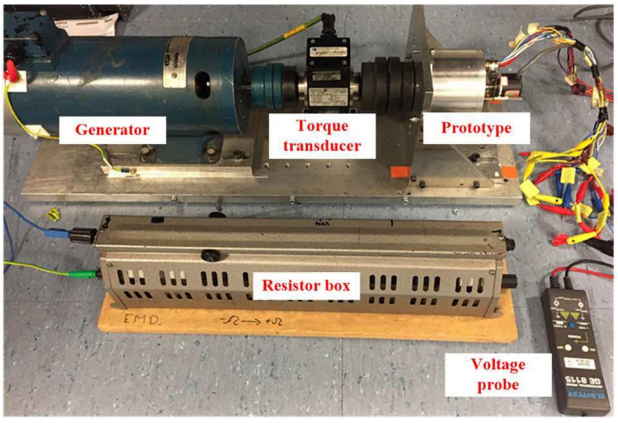

Fig. 14. *Photos of test rig.*

Table 7 FEA predicted and measured peak-values of inductances of prototype 6s/4r VFRM

Inductances	FEA	Measurement
Phase self-inductance of armature winding	57.1 mH	55.4 mH
Mutual inductance between armature and field windings	58 mH	56.5 mH

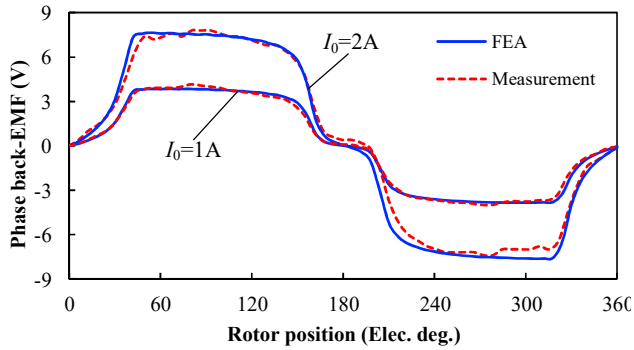

Fig. 15. *Back-EMFs of 6/4 VFRM under 1A and 2A field current excitations.*

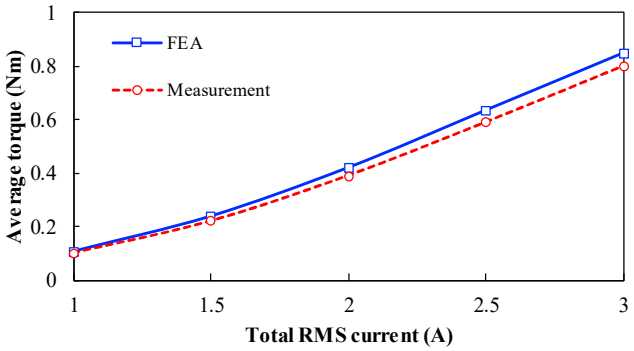

Fig. 16. *Variation of average torque with total RMS current for 6/4 VFRM. (NI_{ratio}=1).*

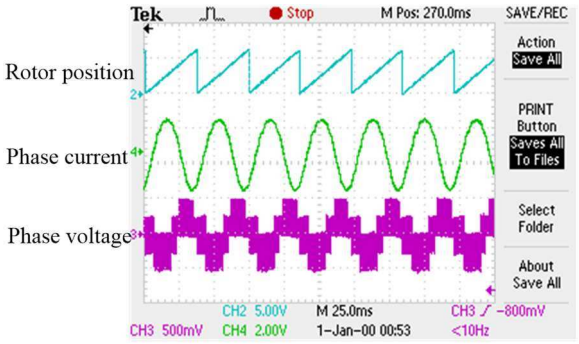

Fig. 17. *Measured rotor position, phase current and phase voltage (I_q=I_f=2A).*

Further, to measure the power factor of prototype, the phase voltage and current are obtained by the voltage probe and current clamp, as shown in Figs. 14 and 17. The voltage signal contains many harmonics, which is mainly due to the PWM. The power factor is then obtained from the phase shift of fundamental components of voltage and current waveforms. Fig. 18 shows the variations of power factor with AC and DC currents. As expected, the higher the DC/AC ampere turns ratio is, the higher the power factor will be.

It should be noted that the prototype is a small scale machine, which is manufactured only for validation. Therefore, the influence of phase resistance on power factor,

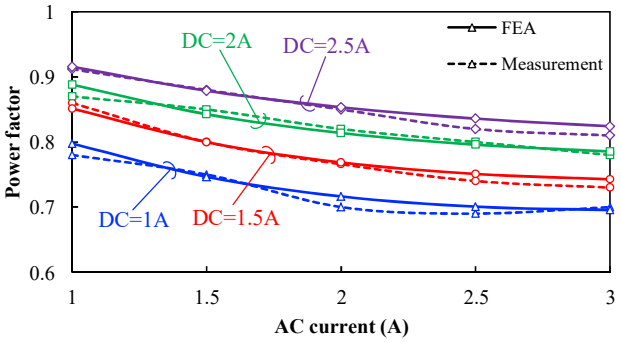

Fig. 18. *Measured and FEA predicted power factor under different load condition (I_d=0, rotating speed is 400rpm).*

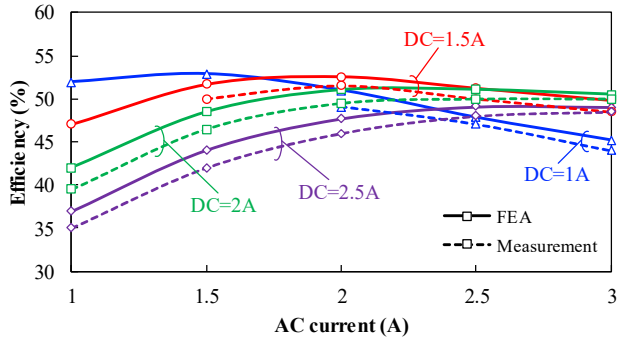

Fig. 19. *Measured and FEA predicted efficiency under different load condition (I_d=0, rotating speed is 400rpm).*

which is usually negligible in large scale machine, should be taken into account during this experiment. The power factor when I_d=0 can be expressed as:

$$pf = \frac{U_q}{\sqrt{U_d^2 + U_q^2}} = \frac{1}{\sqrt{1 + \left(\dfrac{\omega\Phi_q}{\omega\Phi_f + RI_q}\right)^2}} \tag{26}$$

It can be seen that due to the relatively large magnitude of RI_q in small scale machine, the power factor is increased significantly, especially for low speed operation. Moreover, for the same DC/AC ampere turns ratio and rotating speed, RI_q is linearly proportional to I_q, whereas Φ_q and Φ_f are constrained by the core saturation. As a result, the larger the excitation is, the higher the power factor will be, as confirmed in Fig. 18. Nevertheless, the revealed influence of DC/AC winding ampere turns ratio on power factor can still be clearly observed in the test of the prototype.

Finally, the efficiency of the prototype machine are measured by calculating the input power and output power, i.e.,

$$Eff. = \frac{T\Omega_r}{3UI_a \cos\varphi} \tag{27}$$

The results are shown in Fig. 19. The measured results are smaller than the FEA prediction because the mechanical loss is not taken into account. By comparing Figs. 18 and 19, it can be found that the power factor is indirectly related to the efficiency. A high power factor does not necessarily result in a high efficiency since the copper loss and iron loss vary with load condition.

7. Conclusion

This paper analyzes the power factor of VFRMs. The analytical expression of power factor is derived and the relationship between the design parameters and the power

factor is identified. The power factor of VFRMs is found to be influenced by three predictable ratios, i.e.

(a) Rotor permeance ratio. It is a ratio between the 1st and dc components of rotor permeance. The smaller the rotor pole arc and airgap length are, the higher the power factor is

(b) Stator/rotor pole ratio. It is a ratio related to stator/rotor pole number and the winding factor. The smaller the rotor pole number is, the higher the power factor will be. In addition, the VFRMs with concentrated winding has higher power factor than those with distributed winding.

(c) DC/AC winding ampere turns ratio. The larger this ratio is, the higher the power factor will be.

The low power factor issue in VFRM is mainly due to the weak coupling between armature and field windings caused by the modulation effect of the salient rotor. The most effective way for power factor regulation is to adjust the DC/AC ampere turns ratio, albeit with degraded torque/copper loss ratio. Based on this, a design method is developed to take the power factor into account for VFRMs. All the analyses are verified by FEA and experiment.

The work presented in this paper not only explains the underlying mechanism of power factor in VFRM from the MMF and permeance perspective, but also provides a potential method to analyze the power factor of other kinds of stator PM-excited or DC-excited machines with doubly-salient core structure.

8. References

[1] C. C. Chan: 'The state of the art of electric and hybrid vehicles', *Proc. IEEE*, 2002, **90**, (2), pp. 247–275

[2] T.M. Jahns, V. Blasko: 'Recent advances in power electronics technology for industrial and traction machine drives', *Proc. IEEE*, 2002, **89**, (6), pp. 963–975

[3] R. S. Arashloo, J. L. R. Martinez, M. Salehifar, M. Moreno-Eguilaz: 'Genetic algorithm-based output power optimization of fault tolerant fivephase brushless direct current drives applicable for electrical and hybrid electrical vehicles', *IET Elect. Power Appl.*, 2014, **8**, (7), pp. 267–277

[4] W. Lajnef, J.-M. Vinassa, O. Briat, H. El Brouji, S. Azzopard, E. Woirgard: 'Quantification of ageing of ultracapacitors during cycling tests with current profile characteristics of hybrid and electric vehicles applications', *IET Elect. Power Appl.*, 2007, **1**, (5), pp. 683-689

[5] A. M. EL-Refaie: 'Fractional-slot concentrated-windings synchronous permanent magnet machines: opportunities and challenges', *IEEE Trans. Ind. Electron.*, 2010, **57**, (1), pp. 107–121

[6] K. T. Chau, C. C. Chan, C. Liu: 'Overview of permanent-magnet brushless drives for electric and hybrid electric vehicles', *IEEE Trans. Ind. Electron.*, 2008, **55**, (6), pp. 2246–2257

[7] D. Dorrell, L. Parsa, I. Boldea: 'Automotive electric motors, generators, and actuator drive systems with reduced or no permanent magnets and innovative design concepts', *IEEE Trans. Ind. Electron.*, 2014, **61**, (10), pp.5693-5695

[8] I. Boldea, L. N. Tutelea, L. Parsa, D. Dorrell: 'Automotive electric propulsion systems with reduced or no permanent magnets: an overview', *IEEE Trans. Ind. Electron.*, 2014, **61**, (10), pp. 5696-5711

[9] T. Fukami, Y. Matsuura, K. Shima, M. Momiyama, M. Kawamura: 'Development of a low-speed multi-pole synchronous machine with a field winding on the stator side', *Proc. Int. Conf. Elect. Mach.* (ICEM), Rome, Italy, Oct. 2010, pp. 1–6

[10] P. J. Lawrenson, J. M. Stephenson, P. T. Blenkinsop, J. Corda, N. N. Fulton: 'Variable-speed switched reluctance motors', *Inst. Elect. Eng. Elect. Power Appl.*, 1980, **127**, (4), pp. 253–265

[11] X. Liu, Z. Q. Zhu, Z. P. Pan: 'Analysis of electromagnetic torque in sinusoidal excited switched reluctance machines having DC bias in excitation', *Proc. Int. Conf. Elect. Mach.* (ICEM), Marseille, France, Sept. 2012, pp. 2882-2888

[12] L. R. Huang, Z.Q. Zhu, J.H. Feng, S.Y. Guo, J.X. Shi, W.Q. Chu: 'Analysis of stator/rotor pole combinations in variable flux reluctance machines using magnetic gearing effect', *IEEE Energy Conversion Congress and Exposition* (ECCE), Cincinnati, US, Oct. 2017, pp. 3187-3194

[13] X. Liu, Z. Q. Zhu, M. Hasegawa, A, Pride, R. Deodhar: 'Vibration and noise in novel variable flux reluctance machine with DC-field coil in stator', *Proc. Int. Conf. Power Electron. Motion Control* (IPEMC), Harbin, China, Jun. 2012, pp.1100-1107.

[14] L.R. Huang, J.H. Feng, S.Y. Guo, J.X. Shi, W.Q. Chu, Z.Q. Zhu: 'Analysis of torque production in variable flux reluctance machine', *IEEE Trans. Energy Convers.*, 2017, **32**, (4), pp. 1297-1308

[15] M. Cheng, P. Han, W. Hua: 'General airgap field modulation theory for electrical machines', *IEEE Trans. Ind. Electron.*, 2017, **64**, (8), pp. 6063-6074

[16] Z. Q. Zhu, W. Q. Chu, Y. Guan: 'Quantitative comparison of electromagnetic performance of electrical machines for HEVs/EVs', *CES Trans. on Elec. Machines and Systems*, 2017, **1**, (1), pp. 37-47

[17] S. Jia, R. Qu, J. Li, Y. Chen: 'Comparison of stator DC-excited vernier reluctance machines with synchronous reluctance machines', *IEEE Electric Machines & Drives Conference* (IEMDC), Coeur d'Alene, US, May 2015, pp. 649-655

[18] Y. Wang, D. Ionel, D. G. Dorrell, S. Stretz: 'Establishing the power factor limitations for synchronous reluctance machines', *IEEE Trans. Magn.*, 2015, **51**, (11), Jun. 2015

[19] M. R. Harris, G. H. Pajooman, S. M. Abu Sharkh: 'The problem of power factor in VRPM (transverse-flux) machines', *Proc. 8th IEE EMD Conf.*, Cambridge, UK, Sept.1997, pp. 386–390

[20] Jaime Renedo Anglada, Suleiman M. Sharkh: 'Analytical calculation of the torque produced by transverse flux machines', *IET Elect. Power Appl.*, 2017, **11**, (7), pp. 1298-1305

[21] J. R. Anglada, S. M. Sharkh: 'An insight into torque production and power factor in transverse-flux machines ', *IEEE Trans. Ind. App.*, 2017, **53**, (3), pp. 1971-1977

[22] Y. Zhao, J. Chai: 'Power factor analysis of transverse flux permanent machines', *International Conference on Electrical Machines and Systems* (ICEMS), Nanjing, China, Jan. 2006, pp. 1-4

[23] Y. Gao, R. Qu, D. Li, J. Li: 'A Novel hybrid excitation flux reversal machine for electric vehicle propulsion', *IEEE Vehicle Power and Propulsion Conference* (VPPC), Hangzhou, China, Oct. 2016, pp. 1-6

[24] S. Jia, R. Qu, J. Li: 'Analysis of the power factor of stator DC-excited vernier reluctance machines', *IEEE Trans. Magn.*, 2015, **51**, (11)

[25] D. Thyroff, C. Hittinger, I. Hahn: 'Analytic power factor calculation for vernier machines with concentrated windings', *IEEE International Electric Machines and Drives Conference* (IEMDC), Miami, USA, May. 2017, pp. 1-6

[26] D. Li, R. Qu, and J. Li: 'Topologies and analysis of flux-modulation machines', *Proc. IEEE Energy Convers. Congr. Expo.* (ECCE), Montreal, Canada, Sept. 2015, pp. 2153–2160

[27] X. Zhang, X. Liu, J. Liu, and Z. Chen: 'Analytical investigation on the power factor of a flux-modulated permanent-magnet synchronous machine', *IEEE Trans. Magn.*, 2015, **51**, (11), Nov. 2015.

[28] T. A. Lipo: 'Analysis of Synchronous Machines' (Boca Raton, FL, USA: CRC Press, 2008, 2nd ed.)

[29] B. Heller and V. Hamata: 'Harmonic Field Effects in Induction Machines' (Amsterdam, the Netherlands: Elsevier, 1977)

[30] Z. Q. Zhu, B. Lee, and X. Liu: 'Integrated field and armature current control strategy for variable flux reluctance machine using open winding', *IEEE Trans. Ind. App.*, 2016, **52**, (2), pp. 1519-1529

[31] L.R. Huang, J.H. Feng, S.Y. Guo, J.X. Shi, W.Q. Chu, and Z.Q. Zhu: ' Fast design method of variable flux reluctance machines', *CES Transactions on Electrical Machines and Systems*, 2018, **2**, (1), pp. 152-159